Background free imaging of upconversion nanoparticle distribution in human skin

Zhen Song
Yuri G. Anissimov
Jiangbo Zhao
Andrei V. Nechaev
Annemarie Nadort
Dayong Jin
Tarl W. Prow
Michael S. Roberts
Andrei V. Zvyagin

Background free imaging of upconversion nanoparticle distribution in human skin

Zhen Song,[a] Yuri G. Anissimov,[b] Jiangbo Zhao,[a] Andrei V. Nechaev,[c] Annemarie Nadort,[a,d] Dayong Jin,[a] Tarl W. Prow,[e] Michael S. Roberts,[f,g] and Andrei V. Zvyagin[a]

[a]Macquarie University, Department of Physics and Astronomy, MQ Biofocus Research Centre, Sydney, NSW 2109, Australia
[b]Griffith University, School of Biomolecular and Physical Sciences, QLD, Australia
[c]Lomonosov Moscow State University of Fine Chemical Technologies, HTBAS Department, 86 Vernadskogo Ave., Moscow, 119571, Russia
[d]University of Amsterdam, Department of Biomedical Engineering and Physics, Academic Medical Center, P.O. Box 22700, 1100 DE Amsterdam, The Netherlands
[e]The University of Queensland, School of Medicine, Princess Alexandra Hospital, Dermatology Research Centre, Brisbane, QLD, Australia
[f]The University of Queensland, School of Medicine, Therapeutics Research Centre, Brisbane, QLD 4102, Australia
[g]University of South Australia, School of Pharmacy & Medical Sciences, Adelaide, SA 5001, Australia

Abstract. Widespread applications of nanotechnology materials have raised safety concerns due to their possible penetration through skin and concomitant uptake in the organism. This calls for systematic study of nanoparticle transport kinetics in skin, where high-resolution optical imaging approaches are often preferred. We report on application of emerging luminescence nanomaterial, called upconversion nanoparticles (UCNPs), to optical imaging in skin that results in complete suppression of background due to the excitation light back-scattering and biological tissue autofluorescence. Freshly excised intact and microneedle-treated human skin samples were topically coated with oil formulation of UCNPs and optically imaged. In the first case, 8- and 32-nm UCNPs stayed at the topmost layer of the intact skin, stratum corneum. In the second case, 8-nm nanoparticles were found localized at indentations made by the microneedle spreading in dermis very slowly (estimated diffusion coefficient, $D_{np} = 3\text{--}7 \times 10^{-12}$ cm$^2 \cdot$ s^{-1}). The maximum possible UCNP-imaging contrast was attained by suppressing the background level to that of the electronic noise, which was estimated to be superior in comparison with the existing optical labels. © 2012 Society of Photo-Optical Instrumentation Engineers (SPIE). [DOI: 10.1117/1.JBO.18.6.061215]

Keywords: upconversion nanoparticle; human skin; transdermal transport; sunscreens; pharmacokinetics; nanotoxicology; bio-nanotechnology.

Paper 12574SS received Aug. 31, 2012; revised manuscript received Oct. 29, 2012; accepted for publication Oct. 31, 2012; published online Nov. 27, 2012.

1 Introduction

The rapidly emerging area of nanotechnology has provided a new impetus to life sciences by way of introducing new tools and techniques.[1] Among these, molecular trafficking in cells and diagnosis of pathological tissue sites *in vivo* tagged with luminescent nanomaterials have demonstrated powerful imaging potential of nanotechnology.[2–4] Targeted drug and gene delivery by means of nanoparticle (NP) vehicles[5] bioconjugated with targeting molecules, such as receptor ligands, antibodies, peptides and metabolites represents another promising application scope of nanomaterials.[6,7] At the same time, the widespread applications of nanotechnology in daily life (cosmetic products) and medical practices (pharmaceutical products) have raised several concerns on the nanomaterial potential hazards due to their unpredictable fate in mammalian organisms and environment, demanding systematic studies.[8,9] Recently emerged nanotoxicology addresses these issues. In particular, nanomaterial absorption rate in biological tissue, and associated toxicological consequences of this absorption are the key problems. Skin represents the organ, which is the most exposed to this potential nanotechnology assault. Therefore, assessment of nanomaterial absorption in skin represents an important research goal.[10–12]

Nanoparticle skin penetration occurs predominantly via intercellular and/or trans-appendageal pathways. NP skin permeability depends on the NP properties, such as size, shape, surface functional groups, surface charge.[9,13] Skin properties can profoundly affect NP penetration. For example, pathologically modified skin (e.g., melanoma lesion) is considerably more permeable to NPs. Chemical (skin enhancers) and physical (ultrasound, massage) treatments of skin promote nanomaterial uptake in skin.[13–17] Investigation of skin permeability versus these parameters will provide valuable knowledge on how to promote or avoid NP penetration in skin.

Among many methods of assaying NP penetration in skin, optical imaging methods stand out due to their noninvasiveness, high sensitivity, and high spatial resolution. Indeed, in optical imaging of nanoparticle distribution in skin, *in vitro* and *in vivo*, including quantum dots[13] and zinc oxide,[12] NPs impregnated with organic fluorescent dye have been successfully demonstrated.[18] However, the existing nanomaterials have several shortcomings. Organic fluorescent dyes sealed in the NP matrix are still prone to photobleaching, and have low efficiency in the infrared (IR) spectral range. Cytotoxicity of quantum dots is hotly debated; their luminescence is intermittent (blinking), and susceptible to environmental perturbations.[19–21] The existing nanomaterials are characterized by relatively broad emission and suboptimal signal-to-background ratio, termed contrast.

Address all correspondence to: Zhen Song, Macquarie University, MQ Biofocus Research Centre, Sydney, NSW 2109, Australia. Tel: +61-2-98507760; Fax: +61-2-98508115; E-mail: zhen.song@mq.edu.au

First, the vast majority of fluorescent probes are excited by light in the ultraviolet (UV) or visible range, while the emitted fluorescence signal is detectable in the visible spectral range. However, it is in this spectral range biological tissues absorb and scatter light strongly.[22] Second, the tissue exposure to light in this range induces intrinsic fluorescence of the living biological tissue (termed autofluorescence) caused by the presence of endogenous fluorophores, such as NAD[P]H, FAD, flavin, keratin, etc. (skin autofluorescence).[23] Although signals generated by luminescent NPs and autofluorescence of biological tissue are separable using spectral methods, the practical efficiency of these approaches is limited. Third, multiple scattering of light in the optically turbid medium of biological tissue generates an unwanted signal overhead in the detection channel. These impair the detection sensitivity and contrast in many biomedical imaging scenarios.

In order to counter these shortfalls of the existent luminescent nanomaterials, we demonstrated the application of UCNPs to background-free imaging of nanoparticle penetration in skin. A recent breakthrough in UCNP synthesis[24–26] resulted in nanoparticles with greatly improved luminescence property, measured in terms of conversion efficiency, η_{UC}, i.e., the emission/excitation power ratio. The unique photophysical properties of UCNPs were expected to allow almost complete suppression of the biological tissue background that may lead to the ultimate single nanoparticle photodetection sensitivity.

Photon upconversion is a nonlinear process manifested by conversion of the longer-wavelength excitation to shorter-wavelength emission. The mechanism is based on the sequential absorption of two or more photons by the metastable long-lived energy state, as shown in Fig. 1 (adapted from Ref. 27), which can be induced by relatively low-intensity ($1–10^3$ W/cm^2) continuous-wave excitation.[28] This process differs markedly from simultaneous two-photon absorption (occurs via a virtual energy level) stimulated by the excitation intensity as high as $>10^5$ W/cm^2 that is usually realized by means of a complex and expensive femtosecond pulsed laser.[29] The majority of the upconversion processes involve photon absorption mediated by the dopant ions know as sensitizers, followed by nonradiative energy transfer from the sensitizer to another dopant ion knows as an activator, culminating in the energy transfer upconversion. The latter process involves a pair of the sensitizer and activator ions excited to the intermediate excited levels.[30] The activator can be transferred to the next excited energy level at the expense
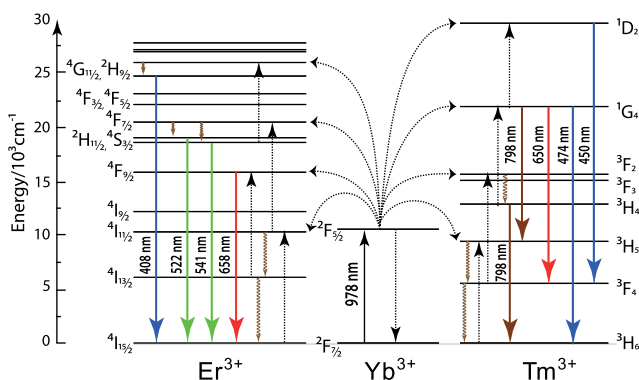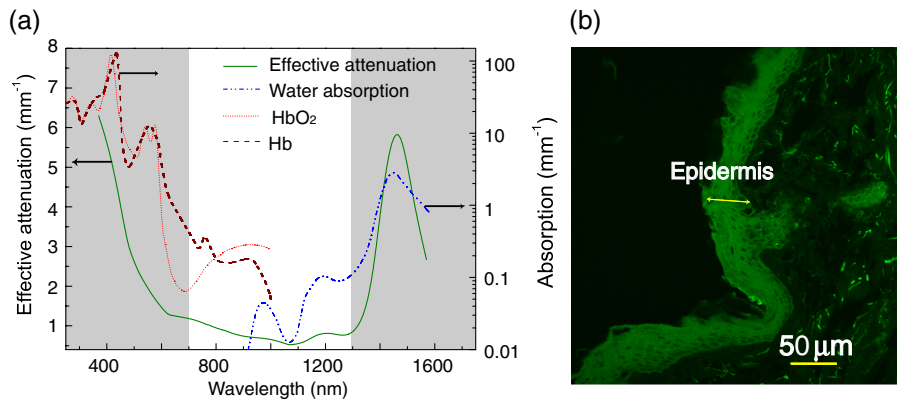
of the participating sensitizer decaying to the ground state. Materials that contain lanthanide and transition-metal ions feature several metastable levels, and often exhibit upconversion phosphorescence, also referred to as luminescence.

The most popular UCNP represents an inorganic nanocrystal matrix (NaYF$_4$) co-doped with the sensitizer ytterbium (Yb^{3+}) and activator erbium (Er^{3+}) or thulium (Tm^{3+}) rare-earth ions. In the NaYF$_4$: Yb, Tm quantum system, a network of closely spaced Yb-ions sensitizes infrared radiation at a wavelength of 978 nm, and couples the nonradiative resonance energy to neighboring Tm-ions characterized by multiple excited states with exceptionally long (sub-ms) lifetimes. As a result of the energy transfer upconversion, Tm^{3+} radiates at 474 nm (three sequential photons) and 798 nm (two sequential photons) spectral bands (Fig. 1). Since the UCNP excitation/emission process is nonlinear, its conversion efficiency (η_{UC}) increases linearly versus the excitation intensity reaching saturation at the high intensity value of $I_{sat} \sim 10$ to 1000 W/cm^2.[30]

There are two main advantages of UCNPs in the context of biomedical optical imaging. Firstly, the NaYF$_4$: Yb, Tm luminescence band at 798 nm falls into the biological tissue transparency window spectral range [clear area in the gray-shaded plot of Fig. 2(a)]. The absorption of the IR (978 nm) laser light by water constituent of biological sample, such as skin, is compensated by the reduced scattering of bio-tissue. The biological tissue transparency window for skin [Fig. 2(b)] is calculated and presented in Fig. 2(a) in terms of the effective attenuation σ_{eff} (defined as the tissue depth at which incident light intensity is attenuated e fold) versus wavelength. σ_{eff} of skin with such constituents as water, blood etc., was calculated as $\sigma_{eff} = \{3\mu_a[\mu_a + \mu_s(1 - g)]\}^{-1/2}$, where μ_a and μ_s stand for the absorption and scattering coefficients[31] $\mu_s' = \mu_s(1 - g)$—reduced scattering coefficient, g being the anisotropy factor of tissue. The excitation/emission of NaYF$_4$: Yb, Tm (978/798 nm) is hence advantageous for biomedical optical imaging. Secondly, UCNP excitation at 978 nm elicits minimal autofluorescence from biological tissue, and this minute autofluorescence signal is Stokes-shifted to the longer-wavelength, while the upconversion emission is shorter-wavelength shifted allowing efficient spectral separation of the autofluorescence and UCNP luminescence.[32]

The promise of upconversion nanoparticles has been recently demonstrated by imaging of UCNP biomolecular complexes in cell cultures, tissue phantoms, and whole animal models,[34–38] with the autofluorescence background suppressed. The biocompatibility/cytotoxicity and targeted delivery was thougoughly reviewed.[39] These studies have demonstrated the potential of the upconversion luminescence for applications in biomedical imaging. These studies have also revealed shortcomings of UCNP technology. These include limited penetration depth of the UCNP-assisted optical imaging in whole animals because of the requirement for the high excitation intensity usually realised by focussing, which is not readily achievable in turbid biological tissue.[32] Besides, the broad angular distribution of unwanted background photons emerging from biological tissue deteriorates the spectral filtering efficiency of UCNP luminescence (10^6-fold suppression efficiency drops to 10^3-fold).[40] These findings suggest considering target applications, that make use of the key UCNP merits, while evading their shorfalls. One such application is ultrasensitive imaging of UCNPs in thin tissue layers, such as skin. Demonstration of the background-free imaging of nanoparticles in skin will pave a way towards

Fig. 1 Schematic energy level diagram of Ytterbium (Yb^{3+}) ions with participating Erbium (Er^{3+}) or Thulium (Tm^{3+}) ions, respectively. Yb^{3+} and Er^{3+} (Tm^{3+}) serve as the sensitizer and activator, respectively.

Fig. 2 (a) Optical effective attenuation spectrum of living skin tissue (solid green line) dominated by water (H_2O, blue "-⋯-" line), hemoglobin (Hb, brown "- -" line), oxy-hemoglobin (HbO_2, red solid "-" line), proteins (not shown), with the scattering effect taken into account. Biological tissue transparency window ranges from 700 to 1300 nm, visualized as clear area against the gray-shaded area. Calculated based on the published data.[33] (b) Autofluorescence image of human skin under the excitation at 405 nm. The viable epidermis layer is color-coded green and marked by an arrow, with cell nuclei are visible as dark ovals. Dermis, visualized primarily via collagen and elastin bundles, is adjacent to the epidermis extending to the right.

ultrasensitive *in vivo* imaging of NP penetration distribution profile in skin and diffusion kinetics.

The paper scope is as follows. First, UCNP-assisted optical imaging that exhibited complete suppression of the optical excitation and skin autofluorescence background is reported for the first time to the best of our knowledge. Based on this result, the ultimate sensitivity of the UCNP imaging is evaluated and compared with that achievable by using conventional fluorescent dyes. Second, assessment of the basic transport properties of UCNPs, such as permeability and diffusion coefficient, by means of optical imaging of freshly excised human skin topically treated with upconversion nanoparticles formulated in oil, is reported.

2 Materials and Methods

2.1 *Upconversion Nanoparticles*

Two UCNP samples, designated as UC1 and UC2, were used in this study. Both samples represented a fluoride nanocrystal $NaYF_4$ doped with Yb^{3+} ions, UC1 and UC2 co-doped with Er ($NaYF_4$: Yb, Er) and Tm ($NaYF_4$: Yb, Tm) ions, respectively. The mean diameters of the oleic acid-capped nanoparticles UC1 and UC2 were 32 and 8 nm, respectively. The luminescence emission spectra of the samples are shown in Fig. 3. The UC1 sample features multiple narrow spectral

bands forming green and red spectral multiplets in the visible spectrum. The UC2 sample features a narrow IR band centered at a wavelength of 798 nm, in addition to a blue emission band centered at 474 nm. Note that the IR band of UC2 falls within the biological tissue transparency window.

A modified oxygen-free hydrothermal protocol was used for the synthesis of UCNP samples,[41] which was reported to produce mono-dispersed particles with controllable sizes and high crystal quality. The UC1 sample ($NaYF_4$: Yb, Er, mean-sized 32 nm) was synthesized using a two-step procedure, where the molar concentrations of Yb and Er were chosen as 18% and 2%, respectively.

Step 1 200 mL of aqueous solution of $LnCl_3$ (1.0 mM, Ln = Y, Yb, Er) was mixed with oleic acid (6 mL) and octadecane (ODE) (15 mL) in a 100-mL three-neck round-bottom flask. The mixture was degassed under argon gas flow and heated to 150°C for 30 min to form a clear, light yellow solution, followed by cooling to room temperature. The solution was magnetic-stirred during this process. 10 mL of methanol solution containing NH_4F (0.1481 g) and NaOH (0.1 g) was added and stirred for another 30 min. Then, the solution was slowly heated and maintained at 110°C until methanol and residual water were not completely removed, while the flask was kept unsealed under the continuous argon flow.
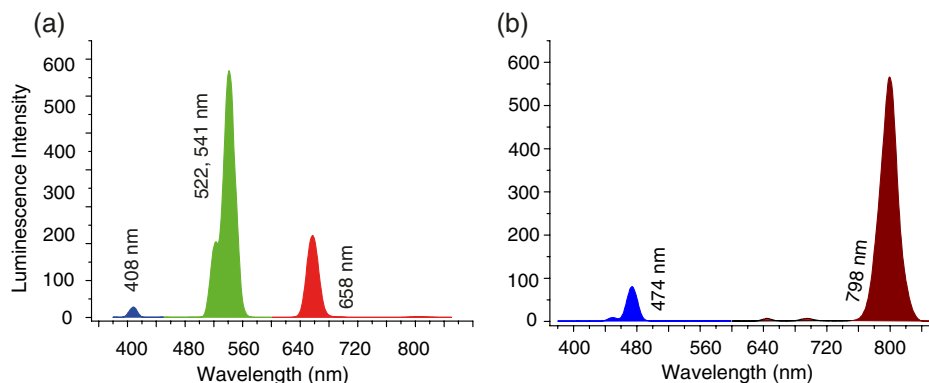
Fig. 3 The luminescence spectra of (a) $NaYF_4$: Yb, Er (UC1) and (b) $NaYF_4$: Yb, Tm (UC2) nanomaterials.

Step 2 After 30 min, the reaction mixture was sealed again, purged with argon, quickly heated to 320°C for 1 h, and cooled down by natural ventilation. Subsequently, acetone was added to precipitate the nanocrystals. The final $NaYF_4$:Yb, Er nanocrystals were re-dispersed in 5 mL of cyclohexane after washing with cyclohexane/acetone two times.

The sample UC2 ($NaYF_4$:Yb, Tm, mean-sized 8 nm) was synthesized following the same procedure, as described above, except at Step 2, a lower temperature of 280°C and shorter reaction time of 30 min were used.

2.2 Characterization

Transmission electron microscope (TEM) measurements of UCNP size and morphology were performed using a Philips CM10 TEM with Olympus Sis Megaview G2 Digital Camera. The samples for TEM analysis were prepared by placing a drop (20 μL) of the dilute suspension of nanocrystals onto formvar-coated copper grids (300 meshes) and allowing them to dry in a desiccator at room temperature. Size distributions were validated by dynamic light scattering (DLS) technique using Zetasizer system ZS90 (Malvern Instruments Ltd., United Kingdom) equipped with helium-neon laser (632.8 nm). The upconversion luminescence spectra of the colloidal solutions in quartz cuvettes with 10 mm path length were acquired using a Fluorolog-Tau3 spectrofluorometer (Jobin Yvon-Horiba) illuminated with an external 978-nm continuous-wave diode laser with maximum achievable power of ~1.2 W.

2.3 Fresh Skin Franz Cell Assay

Human skin was acquired from the liposuction procedure at Princess Alexandra Hospital, Brisbane. All experiments conducted on human subjects were carried out with the approval of Princess Alexandra Hospital Human Ethics Research Committee (Approval no. 097/090, administered by the University of Queensland Human Ethics Committee). Freshly excised skin was processed one day following the surgery, which ensured that the skin viability was largely preserved.[42] The skin sample was divided into six patches. Each patch was fixed on a Franz cell, which is a common tool for evaluation of transdermal solute transport, whose receptor phase is usually filled with a saline or PBS buffer to keep the membrane (skin) moist and the entire cell is kept at 35°C to achieve a skin surface temperature of 31°C, in order to maintain physiologically relevant conditions.[43] The skin patch treatment exposure area was chosen as 1.33 cm^2, and the UCNP material was applied in quantity of 0.8 mg formulated in 250-μL capric/caprylic triglyceride (CCT) oil in similarity with many cosmetic formulations available on the market. Several selected skin sites were produced with microneedle pretreatment, in order to promote UCNP penetration into the deeper layers of skin, typically, dermis. The geometrical size of the microneedle arrays was $700 \times 250 \times 50$ μm in terms of its length, width, and thickness, respectively. There were three microneedles per 5-mm plate. The plates were assembled in banks of two with 2-mm spacing. A LaserPro S290 laser milling machine was used to cut the 50-μm thick 304 stainless steel sheet to the microneedle specifications. Quality control was done on the microneedles before application and the observed configuration was 704 ± 16 μm long and 258 ± 9 μm wide, with a 250-μm long tip angled at 55 deg. After treatment with UCNP (18 h), skin patches were washed thoroughly. The treated skin was frozen and sectioned, along the dermis-stratum corneum plane, into 20-μm thin cross-sections using a microtome, fixed on glass slides, mounted with Antifade Gold (Invitrogen, New York) and covered with 170-μm thick coverslips. All skin processing followed a standard procedure commonly used in therapeutic research avoiding contamination introduced by handling. Based on the data reported elsewhere,[44,45] the microneedle perforated micro-channel dimensions were estimated as follows: depth, 200 μm; surface perforation length, 150 to 200 μm, with negligible surface perforation width.[44] The skin cross-section looked unperturbed 18 h post-microtomed, as observed by Bal et al.[45] in accord with our own observations.

2.4 Wide-Field Epi-Luminescence Optical Microscopy

The optical microscopy system for upconversion luminescence image acquisition was based on the commercial inverted microscope (Olympus IX71, Olympus, Tokyo, Japan), where our home-built illumination module was incorporated. This module transformed the outputs of light sources, coupled to the microscope illumination port via a multimode fiber (Fig. 4), to uniform illumination of the field-of-view at the sample plane. These light sources were an UV-light-emitting diode (mean-wavelength 365 nm) and infrared (IR) continuous wave laser at 978 nm. In brief, the fiber output is imaged at the back focal plane of the objective lens [40 × /1.15 UAPO water-immersion objective lens (Olympus, Tokyo, Japan)], by means of coupling the objective and field lens; whereas an iris (behind the coupling objective) is imaged at the field of view whose area is controlled by the iris aperture. Hence, this circuit represents a Köhler illumination type. The multimode fiber was dithered by a mechanical vibrator leading to speckle averaging at the field of view, which improved the uniformity of the illumination field. An auxiliary illumination module mounted upright was used for acquisition of bright-field images in transmission mode [see, for example, Fig. 5(a)].

Several filter sets were inserted into the microscope illumination and detection paths, including a filter set designed for acquisition of skin tissue autofluorescence and upconversion nanoparticles images excited by the UV (FC6) and IR (FC5)
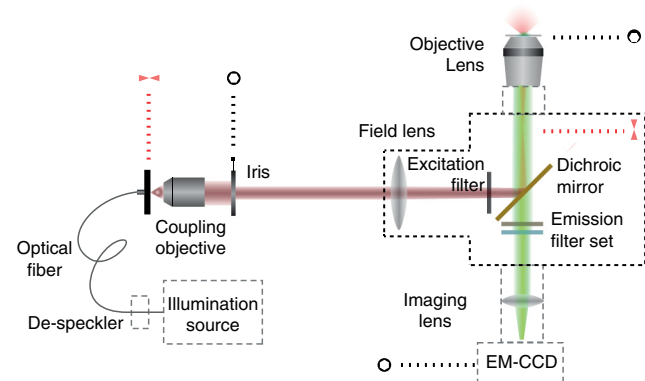
Fig. 4 A schematic diagram of the modified inverted optical microscopy built in-house showing an illumination and detection optical circuits. The infrared (IR) and ultraviolet (UV) excitation sources are multimode fiber-coupled. The fiber output is converted to uniformly illuminated field-of-view at the sample plane. The filter sets are interchangeable depending on the excitation and emission wavelengths. See text for details.
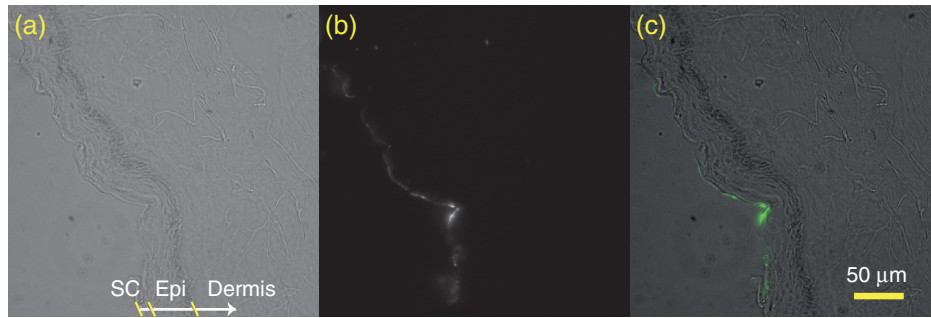
Fig. 5 Optical image of the freshly excised human skin cross-section topically treated with the upconversion nanoparticles (sample UC1, mean size 32 nm) formulated in oil. The images were acquired under (a) bright field, (b) 978-nm laser illuminations; (c) pseudo-color overlay of (a) and (b) highlighting the NP confinement in stratum corneum. SC, Epi, and Dermis designate stratum corneum, viable epidermis, and dermis layers, respectively. Yellow slanted cuts are to guide the eye for delineating these layers.

sources, respectively. FC6 contained a band-pass filter wavelength-centered at 350 nm, with the bandwidth of 50 nm (short notation, 350/50 nm), long-pass dichroic mirror (beam splitter), with the wavelength cut-off at 409 nm, and an additional band-pass 447/60 nm in front of the electron-multiplying charge-coupled device (EMCCD) camera (IXon EMCCD Camera, Andor Technology plc., Belfast, UK). The FC5 filter set comprised a long-pass (cut-off, 850 nm) color-glass filter (RG 850, Edmund Optics Inc., Barrington, New Jersey) in the excitation path to filter the 978-nm excitation source, a single-edge dichroic mirror (FF511-Di01-25 × 36, wavelength cut-off 800 nm; Semrock) reflecting the IR excitation and transmitting the visible emission light to the EM CCD. A blocking-edge short-pass filter (FF01-842/SP-25, wavelength cut-off, 842 nm; Semrock, Rochester, New York) was placed in front of the camera to block the residual IR light. The field of view/spot size and the illumination power intensity were tunable to optimize imaging conditions.

3 Results and Discussion

3.1 Size Distribution

The size distribution of as-synthesized nanomaterials was evaluated by analyzing TEM images of the UCNP samples. Figure 6 shows TEM images of $NaYF_4 : Yb, Er$ (UC1) and $NaYF_4 : Yb$, Tm (UC2) nanoparticles. The size distribution of UC1 [Fig. 6(a)] and UC2 [Fig. 6(b)] samples was estimated as 32 ± 3 and 8 ± 2 nm, respectively, which was consistent with the DLS measurement. As confirmed by the x-ray crystallography

analysis (not shown), the UC1 and UC2 nanoparticles exhibited β- (hexagonal) and α- (cubic) crystal phases, respectively.

Both materials were surface-coordinated with oleic acid functional groups that form a nonpolar hydrocarbon chain monolayer on the surface of nanoparticles that renders them soluble in organic solvents. Specifically, as-synthesized samples were re-dispersed in hexane. UCNPs were also mixable with CCT oil which represented the oil base of cosmetics formulations, producing uniform suspension due to its molecular structure and high viscosity.

3.2 Luminescence Spectra

The luminescence spectrum of the UC1 sample shows three typical emission bands, which are grouped in blue (408 nm), green (522 and 541 nm), and red (658 nm) multiplets [Fig. 3(a)]. Referring to the energy diagram shown in Fig. 1, these transitions are attributed to $^2H_{9/2} \rightarrow ^4I_{15/2}$, $^2H_{11/2} \rightarrow ^4I_{15/2}$, $^4S_{3/2} \rightarrow ^4I_{15/2}$, and $^4F_{9/2} \rightarrow ^4I_{15/2}$, respectively. The green/red and blue multiplets are due to the sequential two and three photon energy absorption, respectively, via the upconversion processes. Note that the peak intensity in the green band is higher than that in the red band. This corroborates our earlier assertion of the β-crystal phase of the sample UC1, and also reports on its high crystal quality, as the green band is highly susceptible to nonradiative relaxation due to bulk crystal and surface defects. The luminescence spectrum of the UC2 sample exhibits two emission bands grouped in blue (474 nm) and infrared (798 nm) multiplets [Fig. 3(b)] due to the sequential three and two photon energy absorption, respectively. As discussed in
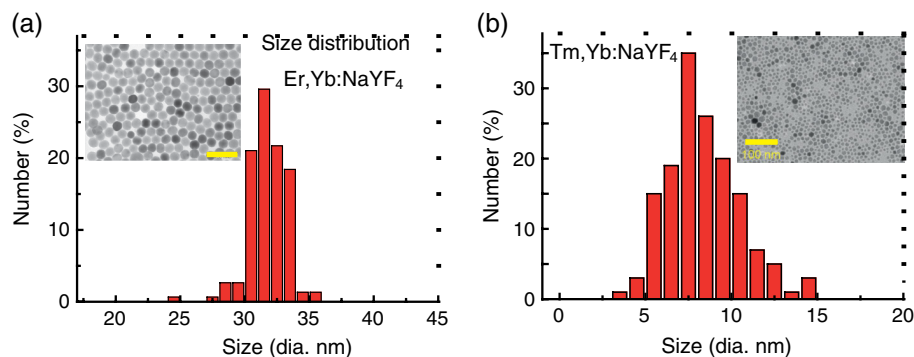
Fig. 6 The size distribution of the upconversion nanoparticle samples: (a) $NaYF_4 : Yb$, Er and (b) $NaYF_4 : Yb$, Tm nano crystal. Insets: Transmission electron microscope (TEM) images of the corresponding samples. Scale bar, 100 nm.

Introduction, this nanomaterial is particularly promising for biomedical imaging applications due to its excitation and emission bands in the near-IR spectral range (978 and 798 nm, respectively) that are situated in the biological tissue therapeutic window [Fig. 2(a)]. It is also anticipated that optical excitation at 978 nm would elicit very little autofluorescence response of the skin tissue. More quantitative assessment of the background due to the autofluorescence and optical excitation back-scattering represents one of the prime goals of this work, and is reported in the experiment described below (Sec. 3.4).

3.3 Imaging of UCNP/Intact Skin

Two UCNP formulations were applied on freshly excised skin patches. These patches were mounted on Franz's cells orienting stratum corneum upwards and immersing the dermal side to buffer solution that was kept at temperature 35°C to sustain the physiological conditions of skin for the duration of the experiment, i.e., 18 h. The formulations based on the UC1 and UC2 samples were applied on intact skin and skin treated with a microneedle device, respectively. Application of this device produced a set of tapered indentations protruding to variable depths in skin, predominantly, in dermis. The subsequent application of the UCNP formulation led to the nanoparticle penetration into these indentations followed by their closure and localization of UC2 NPs in discrete sites in dermis. The skin surface remained intact in between the microneedles. This experimental arrangement allowed testing the intact skin permeability to nanoparticles of mean-sizes 32 and 8 nm; in the latter case, examining intact skin fragments; and, also, diffusion of the 8-nm NPs (UC2) in dermis.

Figure 5 shows the results of our optical imaging of the 32-nm NP (UC1) distribution in intact skin. Figure 5(a) represents the bright filed image and Fig. 5(b) represents the upconversion luminescence image of the same site illuminated with the 978-nm laser. One can clearly see that NPs were confined in the SC layer of skin [demarcated in Fig. 5(c)], with no traces of NPs in the deeper layers (to the right of SC). The second observation emphasizes the high contrast of the UCNP signal under the epi-luminescent imaging conditions. In order to evaluate this imaging contrast quantitatively, we carried out a more comprehensive study of UCNPs in skin by using sample UC2 (NaYF$_4$: Yb, Tm), since its excitation/emission bands were situated in the biological tissue transparency window, i.e., more suitable for biomedical applications.

3.4 Quantitative Evaluation of UCNP Imaging Contrast in Skin

UCNP/skin images were acquired using the modified inverted microscope (described in Sec. 2.4—Wide-Field Epi-Luminescence Optical Microscopy) and illuminated by an UV [365 nm, Fig. 7(a) and 7(d)] light-emitting diode and IR [978 nm, Fig. 7(b) and 7(e)] laser, followed by the image processing and analysis. The radius of the uniformly illuminated area was measured as 280 ± 5 μm for the UV and IR illumination allowing estimation of the excitation intensity at the sample by reading out the optical power at the sample plane. Figure 7, top row, presents the distribution of 8-nm UCNPs in intact skin, i.e., skin fragments that evaded the microneedle treatment. Figure 7, bottom row, presents the UCNP distribution in the microneedle-treated skin. As expected, the nanoparticles stayed in SC of the intact skin, with some accumulation in the skin

fold, whereas the compact localization of UCNPs in deep sites in dermis is clearly observable (Fig. 7, bottom row). As schematically shown in Fig. 7(g), UCNP accumulation sites were located randomly at the same 100-μm-scale depth in dermis, as expected from operation of the microneedle device,[44,45] which corroborated the device-assisted nanoparticle penetration pathway.

A very high Epi-luminescence imaging contrast, defined as the signal-to-background (S/B) ratio, of UCNP versus skin deserves particular attention. It turned out that the background signal was at the level of the cooled EMCCD camera electronic noise, i.e., approximately 60 photoelectrons per pixel per second (60 pe/px · s), with very little dependence on the sample layout, including a clear glass cover slip and fixed thin human skin sample, ambient lighting, and 978-nm laser illumination (see Table 1). The mean signal level of the UCNP was estimated as $S \cong 800$ pe/px · s at the suboptimal excitation intensity of $I_{ex} \cong 11$ W/cm^2 ($I_{ex} \ll I_{sat}$, I_{sat} being the saturation intensity) determined by the available power of the laser source and illumination module throughput. Due to the supra-linear dependence of the UCNP conversion efficiency, η_{UC}, its saturation occurs at the higher intensities, such as 150 W/cm^2 reported by Ref. 46, or 70 W/cm^2 reported in our case,[47] which varies depending on the material characteristics.

In order to place this investigation into the context of fluorescent molecular probe imaging on the biological tissue autofluorescence background, we quantified the autofluorescence signal of our freshly excised skin sample under the UV excitation. The measured average optical background signals from the epidermis and dermis human skin layers amounted to 8.0×10^4 and 2.4×10^4 pe/px · s, respectively, at the UV excitation intensity of $I_{ex} \cong 0.13$ W/cm^2 (Table 1). Note that the autofluorescence signal (comprising contributions from endogenous NAD[P]H elastin, tryptophan, flavins, and porphyrins) was appreciably faded during the 18-h experimental procedure due to the disruption of the metabolic activity of cells in the epidermal and dermal layers.[42] The dermis layer autofluorescence turned out to be dimmer because of the lower abundance of the dominant endogenous fluorophores, NAD[P]H and FAD, and inefficient excitation of the major dermal structures of collagen and elastin at 365 nm.

In order to demonstrate the promise of the molecular probes based on the upconversion nanoparticles for ultrahigh-sensitivity imaging, two imaging scenarios were modeled and compared. Epi-luminescence imaging of a single UCNP and UV organic fluorescent dye [Stilbene 1, (Sb1)] on the experimentally measured skin background were considered, and their contrasts were evaluated. The detected signal, S [pe/px · s] of a single molecular probe is calculated by using the following equation:

$$S = \xi N_{em} \eta \sigma_{abs} I_{ex}, \qquad (1)$$

where σ_{abs}, η, and N_{em} denote the emitter absorption cross-section, conversion efficiency, and number of emitters contributing to the signal sampled by one pixel of the imaging camera, respectively; ξ is a conversion coefficient that combines the objective lens collections efficiency, microscope detection circuit throughput, and EMCCD camera quantum conversion efficiency. For simplicity, ξ is assumed spectrally invariant. In the UCNP model, we consider a NaYF$_4$: Yb, Er particle of the mean diameter of 70 nm, whose photophysical properties were characterized, based on the method reported by Popov et al.[47] Note
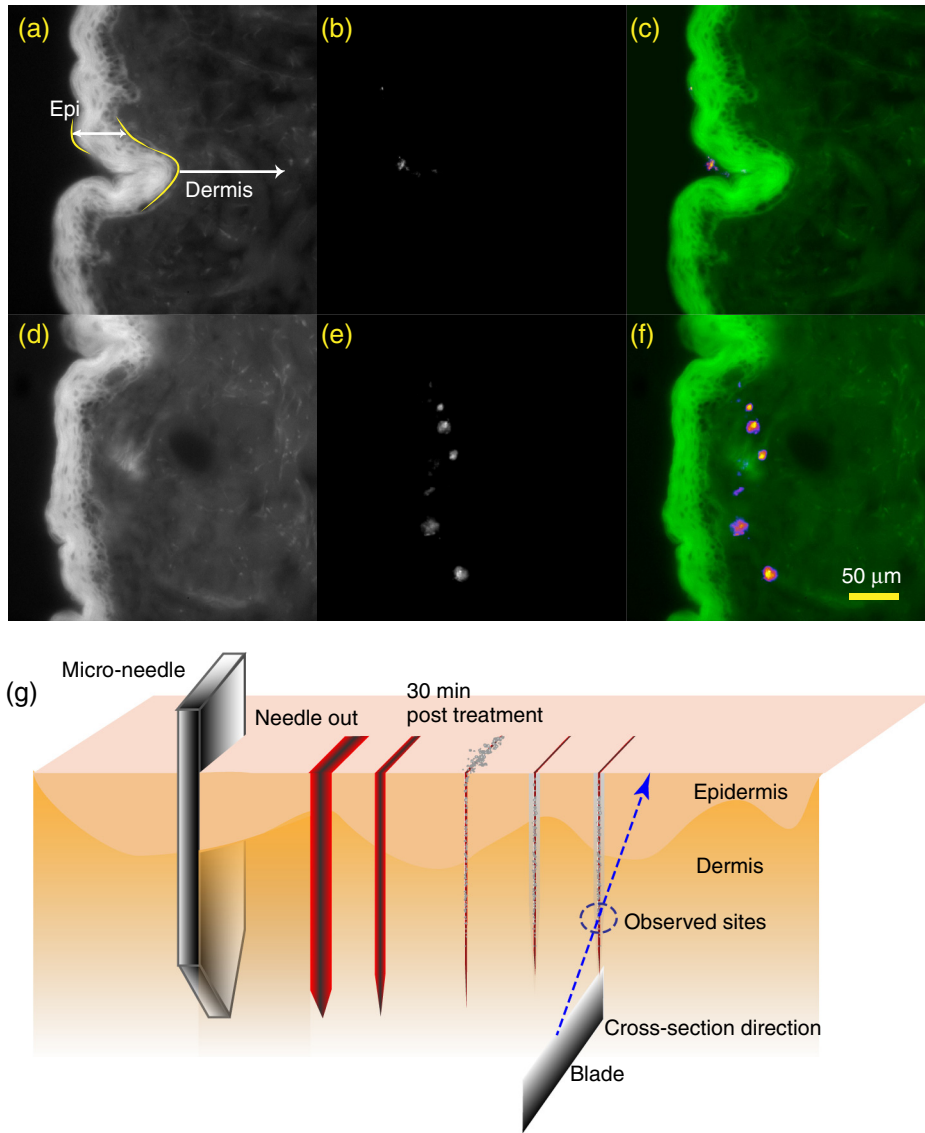
Fig. 7 Eight nanaometer nanoparticle (NaYF$_4$:Yb, Tm, sample UC2) distribution in (top row) intact and (bottom row) microneedle-treated human skin, respectively, following topical application of the upconversion nanoparticle (UCNP) formulated in capric/caprylic triglyceride (CCT) oil. (a), (d), Ultra-violet (UV; 365 nm) excited autofluorescence images of skin; (b), (e) images of UCNPs excited by a 980-nm laser; (c), (f), pseudo-colour overlaid images of (a), (d) showing UCNPs (purple color) in the skin furrow and dermis (green color), respectively. (g) Schematic diagram of the procedure of the application of a microneedle (here, one-blade microneedle, for clarity). From left to right: the microneedle blade is removed from the skin, leaving a perforation that takes the shape of the blade. This cut closes within several minutes followed by application of the formulated upconversion nano-particles that penetrate to dermis through random perforation pores. At the skin preparation stage, thin skin cross-sections are microtomed with a blade, so that a line of randomly distributed UCNP sites at the intersection of the microneedle and microtome blades are clearly observable.

that UCNP's η is a linear function at $I_{ex} \ll I_{sat}$ reaching a pla-teau at $I_{ex} = I_{sat}$, which we assume equal to 70 W/cm^2, and will be used hereafter for the evaluation.[47] The number of Sb1 molecules N_{em}^{Sb1} that make up the imaging contrast S/B, comparable to that of the UCNP was estimated from the follow-ing equation:

$$\frac{S}{B} = \frac{\xi N_{Sb1}\eta_{Sb1}\sigma_{abs}^{Sb1}I_{ex}^{Sb1}}{B_{af}} = \frac{\xi N_{Yb}\eta_{UCNP}\sigma_{abs}^{UCNP}I_{ex}^{UCNP}}{B_{e.n.}}, \quad (2)$$

where B_{af} and $B_{e.n.}$ denote the skin sample autofluorescent signal and EMCCD electronic noise, respectively, as shown in Table 1. Note that the ratio of I_{ex}^{Sb1}/B_{af} is constant in virtue

of the linearity of the Sb1 and endogeneous fluorophore signals versus the excitation intensity, so it suffices to use its experimen-tal value measured at $I_{ex} \cong 0.13$ W/cm^2.

Substituting the tabulated values to Eq. (2), one gets the num-ber of Stilbene 1 molecules of $\sim 1.52 \times 10^5$ that reaches the signal level of one upconversion nanoparticle whose imaging contrast on the skin autofluorescence background is comparable to that of a single UCNP-based molecular probe, see Table 2 (parameters used for this estimation). Such a significant (five orders of magnitude) difference in imaging contrasts is partly due to the least favorable choice of the UV fluorophore. How-ever, in the case of ultrahigh sensitivity imaging of live skin, the background due to the autofluorescence and excitation light

Table 1 Evaluation of UCNPs and freshly excised human skin signals excited by the IR and UV light sources Error was determined based on a standard deviation over the measurements at several pixels.

Excitation source	IR (978 nm)			UV (365 nm)	
Signal origin	UCNP	Epidermis	Electronic noise	Epidermis	Dermis
Signal level (pe/px · s)	$(8 \pm 1) \times 10^2$	84 ± 5	77 ± 5	$(8.0 \pm 0.5) \times 10^4$	$(2.5 \pm 0.3) \times 10^4$

back-scattering can be daunting for a fluorescent organic dye in UV and visible spectral ranges, while UCNP contrast is still expected to be determined by the electronic noise. So, although our comparison is arguably biased, it is not unrealistic for the *in vivo* imaging.

Such an unprecedented contrast of the upconversion nano-materials can be utilized in many challenging optical biological imaging applications. As an example of the utility of this high imaging contrast, we demonstrate the evaluation of the NP diffusion rate in dermis.

3.5 Upconversion Nanoparticle Diffusion in Dermis

Referring to Fig. 7, tight clustering of UCNPs at the microneedle indentation sites suggested anomalously slow diffusion rate of these 8-nm NPs into skin. In order to quantify this observation, we analyzed the transport properties of UCNPs (sample UC2) by fitting our data to the following theoretical model.

The diffusion of the upconversion nanoparticles in dermal tissue outside of a microneedle channel (diameter r_0) of the assumed initial distribution of UCNPs is described by the following diffusion equation in cylindrical coordinates:

$$\frac{\partial}{\partial t} C(r,t) = D \left[\frac{\partial^2}{\partial r^2} C(r,t) + \frac{1}{r} \frac{\partial}{\partial r} C(r,t) \right], \qquad r \geq r_0, \tag{3}$$

where $C(r,t)$ is the NP concentration at time t and distance r from the center of the microneedle, and D is the diffusion coefficient. The UCNP concentration at $r < r_0$ is assumed constant; C_0 imposes the boundary condition $C(r_0,t) = C_0$ at $r = r_0$, and the initial condition, $C(r,0) = 0$, $r > r_0$ of no nanoparticles outside of the channel at $t = 0$.

Equation (3) is readily solved using Laplace transform (see, for example, Ref. 49) yielding the Laplace-domain solution:

$$\hat{C}(r,s) = \frac{C_0}{s} \cdot \frac{K_0 \left(\frac{r}{r_0} \sqrt{s t_d} \right)}{K_0 \left(\sqrt{s t_d} \right)}, \tag{4}$$

where $K_0(x)$ is the modified Bessel function, s is the Laplace variable, and $t_d (= r_0^2/D)$ is the characteristic time of diffusion. Equation (4) for concentration was inverted numerically and fitted to the experimental data using a custom-written code in Python programming language. The numerical inversion was performed using an algorithm described in Ref. 50. As the diameter of the channel produced by the microneedle was not known, two methods of fitting the experimental data were implemented: In Method 1, r_0 was fixed to 3 μm, and C_0 and t_d were found by regression [see Fig. 8(b), blue solid line]. In Method 2, r_0, C_0 and t_d were all determined by regression [Fig. 8(b), red dotted line]. The result of the fitting curve and data is shown in Fig. 8(b) exhibiting good regression quality. The first and second methods yielded the nanoparticle diffusion coefficient of $D_{np} = (3 \pm 0.8) \times 10^{-12}$ cm^2 s^{-1} and $D_{np} = (7 \pm 3) \times 10^{-12}$ cm^2 s^{-1} $(n = 3)$, respectively. This approach provided a relatively tight range for the approximation of the nanoparticle diffusion coefficient in the dermal tissue.

To compare our results with the existing data, we refer to the diffusion rates for different molecules in dermal tissues.[51,52] For example, the diffusion coefficient of hydrocortisone ($MW_{hyd} = 362$ Daltons) in human dermis was reported as $D_{hyd} = (4.3 \pm 0.7) \times 10^{-7}$ cm^2 s^{-1}(50). Assuming that the diffusion coefficient in the dermis behaves similarly to that of water and is proportional to $V^{-0.6}$,[53] where V is the volume of the molecule or nanoparticle, the expected ratio of the diffusion coefficients is:

$$\frac{D_{np}}{D_{hyd}} = \left(\frac{V_{hyd}}{V_{np}} \right)^{0.6} = \left[\frac{MW_{hyd}/(\rho_{hyd} N_A)}{\pi d_{np}^3/6} \right]^{0.6} = 0.03, \tag{5}$$

where $\rho_{hyd}(\approx 1$ g · cm$)$ is the density of hydrocortisone, N_A is Avogadro's number, and d_{np} (8 nm) is the UCNP (UC2) diameter. Using the experimental values for D_{np} and D_{hyd} given above yields a much smaller ratio of about 10^{-5}. Therefore, D_{np} is more than three orders of magnitude less than expected from our evaluation [see Eq. (5)]. Such considerable reduction of the diffusion rate in dermis in comparison with that in

Table 2 Parameters used for comparative estimate of the imaging contrast of Stilbene 1 and a single UCNP, 70 nm in diameter.

	Excitation intensity, I_{ex}, W/cm^2	Absorption cross-section, σ_{abs}, cm^2	Conversion efficiency, η_{UC}	Number of absorbers N[a]	Background, B, pe/px · s
Sb1/skin	0.13	1.74×10^{-16}[b]	0.56[b]	1.52×10^5	1×10^5[c]
UCNP/skin	70	2×10^{-20}	0.01[d]	1.1×10^5	80

[a]For Sb 1, represents calculated molecule numbers; for UCNP, N_{Yb}, calculated number of sensitizer (Yb^{3+}) in the 70-nm particle.
[b]Obtained from Ref. 48.
[c]Averaged over the epidermis/dermis layers of the measured skin sample.
[d]Measured at $I_{ex} = 70$ W/cm^2 based on the method presented in Ref. 47.
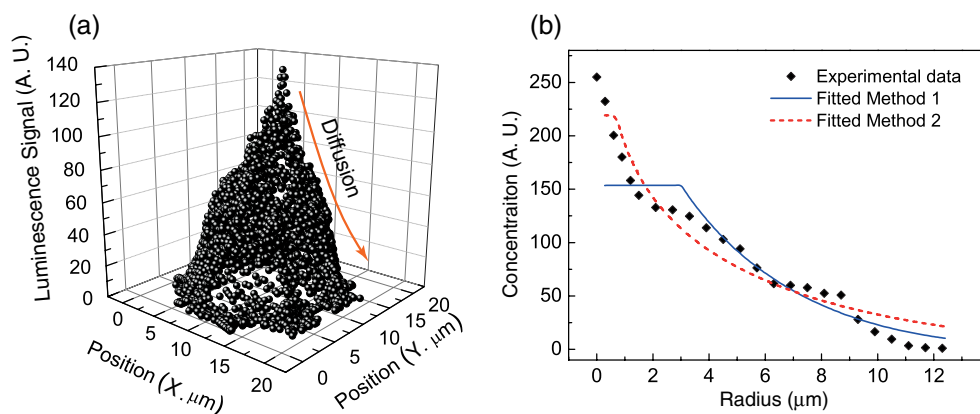
Fig. 8 Diffusion of upconversion nanoparticles from a dermal site located at the tip of microneedle channel. (a) Distribution of upconversion nanoparticle (UCNP) concentration evaluated in terms of photoelectrons per pixel per second versus the x-y pixel coordinate, the peak represents the UCNP counts at the tip of microneedle. (b) Averaged UCNP concentration radial profile (gray diamond scatter) fitted to the diffusion theoretical model (method 1—blue solid line; method 2—red dotted line).

homogeneous medium is not unreasonable, and can be explained by e.g., the binding of UCNPs to immobile fractions (fiber phase) of the dermis. Another potential explanation is the NP size was comparable or larger than the average distance between fibers in the dermis.

The aggregation of UCNPs in skin might be another likely contributor to the UCNP diffusion arrest in dermis. Although our estimation of the NP diffusion rate in skin warrants further study, it demonstrated the potential of the background-free imaging to investigate the useful properties of the nanoparticle transport and distribution in biological tissue, such as skin. The high-contrast, high-sensitivity imaging was instrumental in the acquisition of the low-intensity NP diffusion tail, which would otherwise be obscured by the optical background because of skin autofluorescence and scattering.

4 Conclusions

We reported on the application of upconversion nanoparticles (UCNP) to optical imaging in skin. Demonstration of the complete suppression of background due to the biological tissue scattering and autofluorescence represents the key result of this work. Due to the background level suppressed to that of the electronic noise, the UCNP imaging contrast was pushed to the highest achievable value considering the available excitation intensity. High-sensitivity imaging scenarios cross-comparison between UCNP and UV organic fluorescent dye models demonstrated many orders of magnitude superiority of UCNP, with useful bearings on prospective ultrahigh-sensitivity imaging *in vivo* and quantitative evaluation of long term toxicity effects.

The utility of the background-free imaging of UCNP in skin was demonstrated by investigating nanoparticle transport properties in skin. We found that 8- and 32-nm UCNPs stayed at the topmost layer of the intact skin, stratum corneum. In case of the microneedle treated skin, 8-nm nanoparticles were found confined at the micro-needle indentations in dermis spreading very slowly ($D_{np} = 3$ to 7×10^{-12} cm$^2 \cdot$ s^{-1}). This study holds considerable promise for deployment of the upconversion nanomaterials in optical ultrahigh-sensitivity imaging in thin tissue slices, such as skin, with very realistic prospects of extension to *in vivo* applications.

References

1. C. M. Niemeyer, "Nanoparticles, proteins, and nucleic acids: biotechnology meets materials science," *Angew. Chem. Int. Ed.* **40**(22), 4128–4158 (2001).
2. P. Alivisatos, "The use of nanocrystals in biological detection," *Nat. Biotechnol.* **22**(1), 47–52 (2003).
3. T. A. Kelf et al., "Non-specific cellular uptake of surface-functionalized quantum dots," *Nanotechnol.* **21**(28), 285105 (2010).
4. V. K. A. Sreenivasan et al., "Barstar:barnase—a versatile platform for colloidal diamond bioconjugation," *J. Mater. Chem.* **21**(1), 65–68 (2011).
5. L. Brannon-Peppas and J. O. Blanchette, "Nanoparticle and targeted systems for cancer therapy," *Adv. Drug Del. Rev.* **56**(11), 1649–1659 (2004).
6. N. Yamazaki et al., "Endogenous lectins as targets for drug delivery," *Adv. Drug Del. Rev.* **43**(2, Äì3), 225–244 (2000).
7. A. Becker et al., "Receptor-targeted optical imaging of tumors with near-infrared fluorescent ligands," *Nat. Biotechnol.* **19**(4), 327–331 (2001).
8. G. J. Nohynek et al., "Grey goo on the skin? Nanotechnology, cosmetic and sunscreen safety," *Crit. Rev. Toxicol.* **37**(3), 251–277 (2007).
9. M. J. Osmond and M. J. McCall, "Zinc oxide nanoparticles in modern sunscreens: an analysis of potential exposure and hazard," *Nanotoxicol.* **4**(1), 15–41 (2010).
10. S. E. Cross et al., "Human skin penetration of sunscreen nanoparticles: In-vitro assessment of a novel micronized zinc oxide formulation," *Skin Pharmacol. Physi.* **20**(3), 148–154 (2007).
11. B. Gulson et al., "Small amounts of zinc from zinc oxide particles in sunscreens applied outdoors are absorbed through human skin," *Toxicol. Sci.* **118**(1), 140–149 (2010).
12. A. V. Zvyagin et al., "Imaging of zinc oxide nanoparticle penetration in human skin *in vitro* and *in vivo*," *J. Biomed. Opt.* **13**(6), 064031 (2008).
13. T. W. Prow et al., "Quantum dot penetration into viable human skin," *Nanotoxicol.* **6**(2), 173–185 (2012).
14. T. Mauro et al., "Barrier recovery is impeded at neutral pH, independent of ionic effects: Implications for extracellular lipid processing," *Arch. Dermatol. Res.* **290**(4), 215–222 (1998).

15. J. A. Bouwstra and M. Ponec, "The skin barrier in healthy and diseased state," *Biochim. Biophys. Acta-Biomembr.* **1758**(12), 2080–2095 (2006).

16. T.-R. Kuo et al., "Chemical enhancer induced changes in the mechanisms of transdermal delivery of zinc oxide nanoparticles," *Biomaterials* **30**(16), 3002–3008 (2009).

17. A. P. Popov et al., "Advantages of NIR radiation use for optical determination of skin horny layer thickness with embedded TiO_2 nanoparticles during tape stripping procedure," *Las. Phys.* **16**(5), 751–757 (2006).

18. C. Wu et al., "Multicolor conjugated polymer dots for biological fluorescence imaging," *Acs. Nano.* **2**(11), 2415–2423 (2008).

19. R. Hardman, "A toxicologic review of quantum dots: Toxicity depends on physicochemical and environmental factors," *Environ. Health Perspect.* **114**(2), 165–172 (2006).

20. T. S. Hauck et al., "*In vivo* quantum-dot toxicity assessment," *Small.* **6**(1), 138–144 (2010).

21. D. R. Larson et al., "Water-soluble quantum dots for multiphoton fluorescence imaging *in vivo*," *Science* **300**(5624), 1434–1436 (2003).

22. M. H. Niemz, *Laser-Tissue Interactions: Fundamentals and Applications*, Springer, Berlin; Heidelberg, New York (1996).

23. K. König et al., "*In vivo* drug screening in human skin using femtosecond laser multiphoton tomography," *Skin Pharmacol. Phys.* **19**(2), 78–88 (2006).

24. F. Wang et al., "Tuning upconversion through energy migration in core-shell nanoparticles," *Nat. Mat.* **10**(12), 968–973 (2011).

25. H. X. Mai et al., "High-quality sodium rare-earth fluoride nanocrystals: Controlled synthesis and optical properties," *J. Am. Chem. Soc.* **128**(19), 6426–6436 (2006).

26. H. X. Mai et al., "Highly efficient multicolor up-conversion emissions and their mechanisms of monodisperse $NaYF_4 : Yb$, Er core and core/shell-structured nanocrystals," *J. Phys. Chem. C* **111**(37), 13721–13729 (2007).

27. J. F. Suyver et al., "Upconversion spectroscopy and properties of $NaYF_4$ doped with Er^{3+}, Tm^{3+} and/or Yb^{3+}," *J. Lumines.* **117**(1), 1–12 (2006).

28. S. W. Wu et al., "Non-blinking and photostable upconverted luminescence from single lanthanide-doped nanocrystals," *Proc. Acad. Nat. Sci. USA* **106**(27), 10917–10921 (2009).

29. M. Yu et al., "Laser scanning up-conversion luminescence microscopy for imaging cells labeled with rare-earth nanophosphors," *Anal. Chem.* **81**(3), 930–935 (2009).

30. R. H. Page et al., "Upconversion-pumped luminescence efficiency of rare-earth-doped hosts sensitized with trivalent ytterbium," *J. Opt. Soc. Am. B: Opt. Phys.* **15**(3), 996–1008 (1998).

31. N. Y. Ignatieva et al., "Laser-induced modification of the patellar ligament tissue: Comparative study of structural and optical changes," *Las. Med. Sci.* **26**(3), 401–413 (2011).

32. C. Vinegoni et al., "Transillumination fluorescence imaging in mice using biocompatible upconverting nanoparticles," *Opt. Lett.* **34**(17), 2566–2568 (2009).

33. V. V. Tuchin, *Tissue Optics: Light Scattering Methods and Instruments for Medical Diagnosis*, SPIE, Bellingham, WA (2007).

34. Q. Liu et al., "Sub-10 nm hexagonal lanthanide-doped naluf(4) upconversion nanocrystals for sensitive bioimaging *in vivo*," *J. Am. Chem. Soc* **133**(43), 17122–17125 (2011).

35. Q. Zhan et al., "Using 915 nm laser excited $Tm^{3+}/Er^{3+}/Ho^{3+}$-doped $NaYbF_4$ upconversion nanoparticles for *in vitro* and deeper *in vivo* bioimaging without overheating irradiation," *Acs. Nano.* **5**(5), 3744–3757 (2011).

36. M. Nyk et al., "High contrast *in vitro* and *in vivo* photoluminescence bioimaging using near infrared to near infrared up-conversion in Tm^{3+} and Yb^{3+} doped fluoride nanophosphors," *Nano. Lett.* **8**(11), 3834–3838 (2008).

37. C. T. Xu et al., "Autofluorescence insensitive imaging using upconverting nanocrystals in scattering media," *Appl. Phys. Lett.* **93**(17), 171103 (2008).

38. L. Xiong et al., "High contrast upconversion luminescence targeted imaging *in vivo* using peptide-labeled nanophosphors," *Anal. Chem.* **81**(21), 8687–8694 (2009).

39. F. Wang et al., "Upconversion nanoparticles in biological labeling, imaging, and therapy," *Analyst* **135**(8), 1839–1854 (2010).

40. F. Leblond et al., "Pre-clinical whole-body fluorescence imaging: Review of instruments, methods and applications," *J. Photochem. Photobiol. B: Biol.* **98**(1), 77–94 (2010).

41. G. S. Yi and G. M. Chow, "Water-soluble $NaYF_4 : Yb$, Er(Tm)/$NaYF_4$/polymer core/shell/shell nanoparticles with significant enhancement of upconversion fluorescence," *Chem. Mater.* **19**(3), 341–343 (2007).

42. W. Y. Sanchez et al., "Analysis of the metabolic deterioration of *ex vivo* skin from ischemic necrosis through the imaging of intracellular NAD(P)H by multiphoton tomography and fluorescence lifetime imaging microscopy," *J. Biomed. Opt.* **15**(4), 046008 (2010).

43. M. S. Roberts and K. A. Walters, Eds., *Dermal Absorption and Toxicity Assessment*, Informa Healthcare, New York (2007).

44. H. Kalluri and A. Banga, "Formation and closure of microchannels in skin following microporation," *Pharm. Res.* **28**(1), 82–94 (2011).

45. S. Bal et al., "*In vivo* visualization of microneedle conduits in human skin using laser scanning microscopy," *Las. Phys. Lett.* **7**(3), 242–246 (2010).

46. J. C. Boyer and F. van Veggel, "Absolute quantum yield measurements of colloidal $NaYF_4 : Er^{3+}$, Yb^{3+} upconverting nanoparticles," *Nanoscale* **2**(8), 1417–1419 (2010).

47. A. P. Popov et al., "Upconversion luminophores as a novel tool for deep tissue imaging," in *Novel Biophotonic Techniques and Applications*, H. J. C. M. Sterenborg and I. A. Vitkin, Eds., SPIE, Munich, Germany, p. 80900V (2011).

48. T. M. Stachelek et al., "Detection and assignment of the "phantom" photochemical singlet of trans-stilbene by two-photon excitation," *J. Chem. Phys.* **66**(10), 4540–4543 (1977).

49. H. S. Carslaw and J. C. Jaeger, *Conduction of Heat in Solids*, Clarendon Press, Oxford (1959).

50. L. N. Trefethen, J. A. C. Weideman, and T. Schmelzer, "Talbot quadratures and rational approximations," *BIT* **46**(3), 653–670 (2006).

51. K. Kretsos et al., "Partitioning, diffusivity and clearance of skin permeants in mammalian dermis," *Int. J. Pharm.* **346**(64–79) (2008).

52. Y. G. Anissimov and M. S. Roberts, "Modelling dermal drug distribution after topical application in human," *Pharm. Res.* **28**(9), 2119–2129 (2011).

53. C. R. Wilke and P. Chang, "Correlation of diffusion coefficients in dilute solutions," *AIChE J.* **1**(2), 264–270 (1955).